frontiers in Marine Science

TYPE Original Research
PUBLISHED 15 June 2026
DOI 10.3389/fmars.2026.1764162

Check for updates

OPEN ACCESS

EDITED BY
Toru Miyama,
Japan Agency for Marine-Earth Science and Technology, Japan

REVIEWED BY
Yang Wang,
University of Hamburg, Germany
Piero Bernardo,
University of São Paulo, Brazil

*CORRESPONDENCE
Mara Navarro-Buigues
mara.navarro@ulpgc.es
M. Dolores Pérez-Hernández
mdolores.perez@ulpgc.es

RECEIVED 09 December 2025
REVISED 30 April 2026
ACCEPTED 12 May 2026
PUBLISHED 15 June 2026

CITATION
Navarro-Buigues M, Pérez-Hernández MD, Arumi C, Pelegrí JL, Vélez-Belchí P and Hernández-Guerra A (2026) Property and energy transfer by an Agulhas Ring.
Front. Mar. Sci. 13:1764162.
doi: 10.3389/fmars.2026.1764162

COPYRIGHT
© 2026 Navarro-Buigues, Pérez-Hernández, Arumi, Pelegrí, Vélez-Belchí and Hernández-Guerra. This is an open-access article distributed under the terms of the Creative Commons Attribution License (CC BY). The use, distribution or reproduction in other forums is permitted, provided the original author(s) and the copyright owner(s) are credited and that the original publication in this journal is cited, in accordance with accepted academic practice. No use, distribution or reproduction is permitted which does not comply with these terms.

Property and energy transfer by an Agulhas Ring

Mara Navarro-Buigues[1,2]*, M. Dolores Pérez-Hernández[1,2]*, Cristina Arumi[3], Josep L. Pelegrí[4,5], Pedro Vélez-Belchí[5,6] and Alonso Hernández-Guerra[1,2]

[1]Instituto de Oceanografía y Cambio Global (IOCAG), Universidad de Las Palmas de Gran Canaria (ULPGC), Las Palmas de Gran Canaria, Spain, [2]Océano y Clima, Unidad Asociada ULPGC-CSIC, Consejo Superior de Investigaciones Científicas (CSIC), Las Palmas de Gran Canaria, Spain, [3]Barcelona Supercomputing Center (BSC), Barcelona, Spain, [4]Departament d'Oceanografia Física i Tecnològica, Institut de Ciències del Mar, CSIC, Barcelona, Spain, [5]Océano y Clima, Unidad Asociada ULPGC-CSIC, Universidad de Las Palmas de Gran Canaria (ULPGC), Barcelona, Spain, [6]Centro Oceanográfico de Canarias, Instituto Español de Oceanografía (IEO), Consejo Superior de Investigaciones Científicas (CSIC), Santa Cruz de Tenerife, Spain

We use hydrographic observations in March 2022, combined with drifter and altimetry time series, to investigate the structure and time evolution of an Agulhas Ring (AR). This multi-platform approach enables a comprehensive assessment of the ring's water mass properties, heat and salt anomalies, and energy content, offering insights beyond those available from satellite alone. The anticyclonic AR transported relatively (to the background state) warm (>2°C), salty (>0.3) and low-oxygen (≈35 µmol/kg) Indian Ocean waters into the South Atlantic in its upper core. Its velocity field exhibits a coherent solid-body rotating core (~38 km radius) and a radially decaying baroclinic structure in the periphery. The ratio between rotational and translational speeds shows that the eddy maintains a dynamically trapped core down to at least 595 m, representing a lower bound for its vertical extent. Heat and salt anomalies range from 3.4×10^{19} to 4.9×10^{19} J and from 1.1×10^{12} to 1.5×10^{12} kg, respectively, with annualized transports of 1×10^{-3} – 2×10^{-3} PW and 3.3×10^{-5}–4.7×10^{-5} Sv. Available potential energy (1.9–7.4×10^{15} J) exceeds kinetic energy by two orders of magnitude, indicating a strong dominance of potential energy and a tendency toward instability. The observed weakening and fragmentation of the ring near the Walvis Ridge is consistent with the release of this energy during its evolution. These results show that even after several months of propagation, Agulhas Rings remain dynamically active structures that contribute significantly to the transport of heat, salt, and water masses across the South Atlantic.

KEYWORDS
Agulhas Ring, energetic eddies, Indian Ocean, interocean exchange, South Atlantic Ocean

1 Introduction

The Agulhas Current is the western boundary current of the Indian Ocean, transporting relatively warm and saline waters. As it flows poleward along the coast of South Africa, the current detaches from the continental slope and encounters the Antarctic Circumpolar Current. It then turns sharply counterclockwise, forming the Agulhas Return Current. At this retroflection point (Agulhas Current Retroflection), the current loops back on itself, producing occlusions that trap Indian Ocean waters (Arruda et al., 2014; Clement and Gordon, 1995; Elipot and Beal, 2015; Lutjeharms, 2006; Rae et al., 1996). These occlusions, known as Agulhas Rings (AR), are subsequently advected into the South Atlantic by the northwestward-flowing Benguela Current (Duncombe Rae, 1991; Garzoli and Gordon, 1996; Laxenaire et al., 2018; Schouten et al., 2000). The surface cores of ARs are typically warmer (by up to 5°C) and saltier (by up to ≈1) than the surrounding South Atlantic waters (Garzoli et al., 1999; Gordon et al., 1992; Lutjeharms, 2006, 2007).

Agulhas Rings are among the largest and most energetic eddies in the global ocean, with lifetimes of 3–4 years in the South Atlantic (Byrne et al., 1995; Richardson, 2007). They generally have diameters of 200–400 km and depths down to 1500–2000 m, with some extending as deep as 4500 m (Van Aken et al., 2003). ARs are readily detected by sea level anomaly (SLA), which can exceed 1 m above mean sea level (Gordon and Haxby, 1990). Their properties, however, vary depending on the time elapsed since detachment from the Agulhas Retroflection (Casanova-Masjoan et al., 2017; Lutjeharms, 2006; McDonagh et al., 1999). Typical translational speeds range from 0.06 to 0.17 m/s (≈5–15 km/day), and usually decrease under the influence of bottom topography – such as interactions with the Walvis Ridge – or through encounters with other mesoscale features (Byrne et al., 1995; Garzoli and Gordon, 1996; Gordon and Haxby, 1990; Kamenkovich et al., 1996; Schouten et al., 2000).

After formation, most ARs propagate northwestward under the influence of the Benguela Current (average transport: 26.3 ± 2 Sv; Arumí-Planas et al., 2023). Rings then tend to shift westward between 25° and 35°S, with most of them remaining south of 20°S (Gründlingh, 1995). Garzoli and Gordon (1996) defined the Agulhas Eddy Corridor as extending northwestward to 30°S, after which it diverges northward, whereas Goni et al. (1997) placed the "Ring Corridor" further south (30–40°S), marking a more westward trajectory near 5°E. Mason et al. (2017) also show an eddy corridor flowing northwestward and then shifting to a westward direction after 5°E, between 20° and 25°S.

The interbasin transfer of mass, heat and salt from the South Indian Ocean to the South Atlantic is a key component of the Atlantic Meridional Overturning Circulation (AMOC) (De Ruijter et al., 1999; Duncombe Rae, 1991; Gordon and Haxby, 1990; Van Ballegooyen et al., 1994; Weijer et al., 1999). In particular, the influx of relatively warm, saline Indian Ocean waters enhances surface evaporation in the South Atlantic (Beal et al., 2011). Although the surface thermal signal of ARs is quickly attenuated by strong ocean–atmosphere fluxes in the South Atlantic (Mey et al., 1990; Olson et al., 1992), their sea surface salinity (SSS) and sea surface height (SSH) anomalies persist, making them reliable tracers of ring pathways and evolution (e.g., Byrne et al., 1995; Goni et al., 1997; Laxenaire et al., 2018; Nencioli et al., 2018; Schouten et al., 2000). Statistical analyzes based on Argo floats and satellite observations have significantly advanced our understanding of AR trajectories and surface properties (e.g., Laxenaire et al., 2019), but relatively few *in situ* measurements capture their full vertical structure and energetics.

This study addresses this gap using *in situ* observations collected during the SAGA-34.5S cruise in March 2022 at 34.5-37.1°S, 3.8°E in the South Atlantic. We combine vertical profiles of temperature, salinity, oxygen, nitrates and pH; shipboard velocity observations; biogeochemical and hydrographic data from a Southern Carbon and Climate Observations and Modeling (SOCCOM) float; and satellite altimetry data. Together these datasets enable us to characterize the initial state, vertical structure, and evolution of a recently formed AR. This multi-platform framework allows for a more complete assessment of water mass and energy characteristics than satellite data can provide on their own. Specifically, we ask: (1) How do the vertical structure and energetics of an Agulhas Ring evolve after detachment? (2) What does this evolution tell us about the ring's contribution to inter-ocean exchange?

The paper is organized as follows. Section 2 describes the observational datasets and methodology. Section 3 examines the water mass properties, formation processes, velocity fields, heat and salt anomalies, and the available potential and kinetic energies of the AR. Section 4 presents time series of vertical profiles within the ring as obtained from a SOCCOM float. Section 5 discusses the results and provides conclusions.

2 Data and methods

Hydrographic data were collected during the SAGA-34.5S cruise, conducted between February 1st and March 15th, 2022, aboard the R/V *Sarmiento de Gamboa*. For this study, we selected data from eight hydrographic stations occupied over a short, quasi-synoptic period between 4th and 6th March 2022. Thus, all stations were sampled within about 60 hours, minimizing the temporal aliasing. Assuming a mean AR translation speed of 11 cm/s (Section 3.2), the ring would have displaced approximately 24 km over this period, substantially smaller than its radius of maximum azimuthal velocity R_{max} = 86 km (Section 3.3). We therefore consider the hydrographic section to represent a quasi-synoptic view of the ring structure, although minor asymmetries associated with translation cannot be excluded.

The stations were distributed along two perpendicular transects: a zonal transect (stations 75–77), sampling South Atlantic waters away from the AR, and a meridional transect through the AR (stations 80–84), hereafter referred to as T1-SA and T2-AR, respectively (Figure 1a). At each station, vertical profiles of potential temperature (θ) and salinity were obtained at 2-dbar intervals using a conductivity–temperature–depth (CTD) probe. In addition, water samples were collected for salinity, dissolved oxygen, nitrate, and pH analyzes.

The hydrographic measurements were complemented by continuous near-surface salinity and temperature data from a

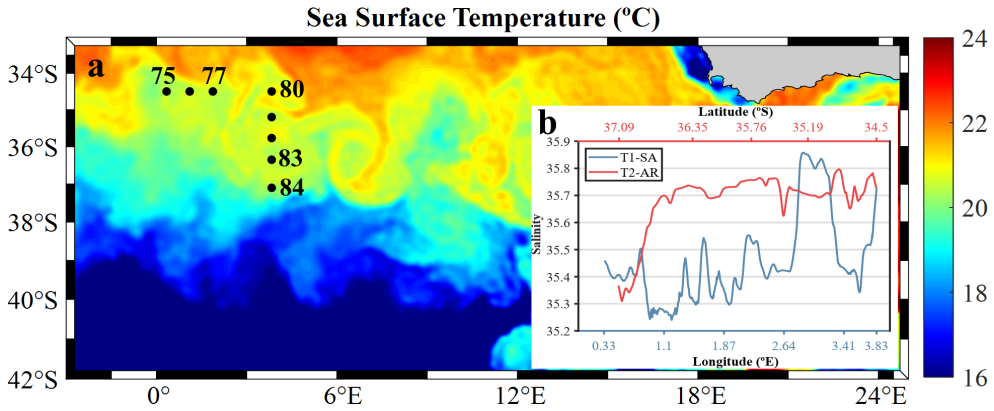

FIGURE 1
(a) Map of the South Atlantic sea surface temperature (SST) on 7 March 2022 (date of the first SOCCOM cycle). Black dots represent hydrographic stations that are divided into two transects; stations 75–77 for T1-SA, and stations 80–84 for T2-AR. **(b)** Sea surface salinity (SSS) from the thermosalinograph for T1-SA and T2-AR, respectively.

thermosalinograph (Figure 1b). Velocity profiles were obtained using a 75 kHz Shipboard Acoustic Doppler Current Profiler (SADCP), which can typically reach from the surface down to depths of 600–900 m depending on acoustic conditions. During our survey, reliable velocity measurements were obtained between 35 and 715 m depth. The SACP data were processed using the CODAS software (https://currents.soest.hawaii.edu/docs/adcp_doc/), resulting in 10m vertical bins. To reduce the influence of small-scale features, the profiles were projected onto a regular grid with 20m vertical resolution and 8 km horizontal spacing. This resolution allows for a robust characterization of the dominant mesoscale spatial structure.

As part of the SOCCOM program (Russell et al., 2014; Sarmiento et al., 2023), a SOCCOM profiler (No. 5906490) was deployed at station 83, near the center of the AR. This float remained trapped within the ring for about 5 months (March–August 2022), providing 10-day profiles of salinity, potential temperature, dissolved oxygen, nitrate, and pH. These data were calibrated using *in situ* measurements from hydrographic station 83 (Figure 1a).

In addition, daily sea level anomaly (SLA) and sea surface temperature (SST) data at 1/4° resolution, spanning 1 June 2021 (ring formation) to 31 August 2022 (when the SOCCOM float exited the ring), were obtained from the Copernicus Marine Service database to track the AR trajectory. Previous studies (Casanova-Masjoan et al., 2017; Goni et al., 1997; Souza et al., 2011) have shown that ARs crossing the South Atlantic can be identified by positive SLA signatures. Accordingly, the ring trajectory was estimated by visually identifying, on each daily SLA map, the location of the maximum positive SLA value enclosed by a closed SLA contour, which defines the eddy center and its outer boundary.

3 Agulhas Ring characteristics

3.1 Water mass properties

The water masses present along transects T1-SA and T2-AR were identified using θ–S diagrams (Figure 2). In addition, the AR is characterized by anomalies in potential temperature, salinity, oxygen, nitrates, and pH (Figure 3), calculated relative to an undisturbed South Atlantic reference state defined by stations 75, 76, and 77 along T1-SA (see Section 1 of Supplementary Material). Property anomalies were obtained by subtracting the mean reference state at each depth from the values measured along T2-AR.

An SST map from 7 March 2022 (Figure 1a) shows the AR along the T2-AR transect, with a weak but discernible surface thermal signature. However, thermosalinograph data (Figure 1b) reveal that surface salinity provides a sharper signal than SST: surface salinities along T2-AR remain above 35.6, whereas waters along T1-SA are fresher. This contrast is also evident in the θ–S diagram (Figure 2), where surface waters (γ^n < 26.14 kg/m^3, i.e. above 100–150 dbar) show similar potential temperatures (16–21 °C) in both transects, but fresher values (≈ 35.4) in T1-SA as compared to Agulhas Water (AGW) along T2-AR (Figures 2, 3a–d). At the surface, temperature anomalies are near zero (Figure 3b), while salinity anomalies are distinctly positive (by ≈0.4; Figure 3d). In the southernmost T2-AR stations, salinity differences vanish, revealing the presence of South Atlantic surface waters (salinity < 35.4; Figure 1b, 3c).

Reference South Atlantic waters in the surface layer (γ^n < 26.14 kg/m^3) are characterized by oxygen concentrations about 230 µmol/kg, potential temperature near 13 °C, salinity near 35.3, and pH_{Tis} = 7.96 (Figures 3a, c, e, i). In contrast, the AR upper core (located near 200 dbar), consisting practically of AGW, is markedly less oxygenated (35 µmol/kg; Figure 3f), warmer (anomalies > 2 °C; Figure 3b), saltier (anomalies > 0.3; Figure 3d), and more alkaline (pH anomaly > 0.04; Figure 3j).

At intermediate depths (100–700 dbar; 26.14 < γ^n < 27.23 kg/m^3), South Atlantic Central Water (SACW) is characterized by relatively warm potential temperatures (6–16 °C; Figures 2, 3a) and salinities of 34.4–35.6 (Figures 2, 3c) (Hernández-Guerra et al., 2019; Stramma and England, 1999). In the eastern South Atlantic, SACW is influenced by Indian Central Water (ICW) advected through the Agulhas Current and ARs (Poole and Tomczak, 1999). ICW, trapped within the AR, has properties similar to SACW but follows a slightly different θ–S relation: ICW is identified for potential temperatures

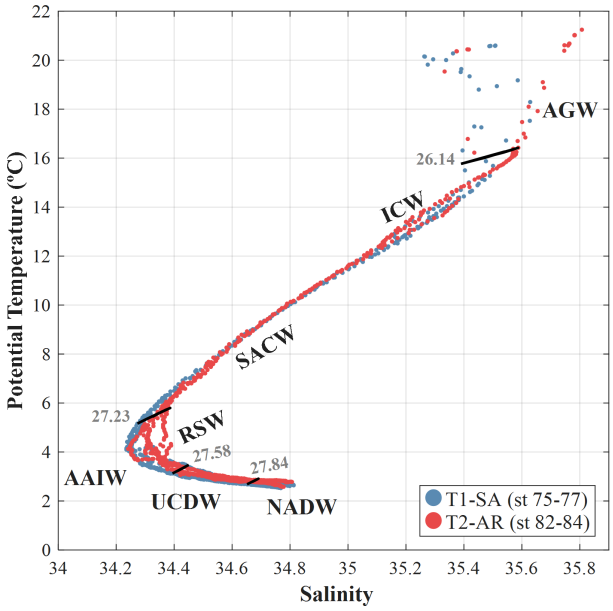

FIGURE 2
θ-S diagrams using CTD data for South Atlantic background waters (T1-SA, blue dots) and the AR waters (T2-AR, red dots). The water masses present are AGW, Agulhas Water; ICW, Indian Central Water; SACW, South Atlantic Central Water; AAIW, Antarctic Intermediate Water; RSW, Red Sea Water; UCDW, Upper Circumpolar Deep Water and NADW, North Atlantic Deep Water. The selected neutral density values separate the water masses.

above 12 °C, whereas SACW dominates in the 7-12 °C range (Figure 2) (Schott and McCreary, 2001). The strongest anomalies occur in the lower AR core (near 500 dbar), consisting of ICW that is warmer (anomaly > 2.5 °C; Figure 3b), saltier (anomaly > 0.3; Figure 3d), nitrate-poor (by 7.5 µmol/L; Figure 3h), and more alkaline (over 0.03; Figure 3j) as compared to SACW. At 500 dbar, reference SACW typically exhibits potential temperatures near 9 °C, salinities near 34.7, nitrate concentrations close to 21 µmol/L, and pH_{Tis} values of 7.89 (Figures 3a, c, g, i).

Below the central waters, between 700 and 1100 dbar ($27.23 < \gamma^n < 27.58$ kg/m^3), Antarctic Intermediate Water (AAIW) is identified by minimum salinities (< 34.3; Figure 2, 3c) and relatively cold potential temperatures (3–5 °C; Figures 2, 3a). In the eastern basin of the South Atlantic, salinity is elevated due to mixing with Indian Ocean intermediate waters entering via the Agulhas Leakage. These waters carry Red Sea Water (RSW), which is slightly warmer (> 0.1 °C) and saltier (> 0.06) than ambient AAIW (Figure 2) (Liu and Tanhua, 2021; Stramma and England, 1999). The Deep Oxygen Maximum (DOM) of South Atlantic waters (about 230 µmol/kg; Figure 3e) occurs between 700–900 dbar, associated with AAIW. Oxygen negative anomalies within the AR core in this layer exceed 27.5 µmol/kg, indicating poorer ventilation relative to the surrounding South Atlantic waters (Figure 3f).

At greater depths (1100–1700 dbar; $27.58 < \gamma^n < 27.84$ kg/m^3), Upper Circumpolar Deep Water (UCDW) is observed, advected northward from Southern Ocean upwelling regions (Stramma and England, 1999). The UCDW tongue is detected near 34.5°S, with potential temperatures about 3 °C and salinities around 34.6 (Figures 2, 3a, c).

3.2 Agulhas Ring trajectory and evolution

The trajectory of the eddy was estimated by tracking the maximum value of local SLA, which represents the center of the AR, using daily altimetry maps (Casanova-Masjoan et al., 2017). Figure 4 shows the formation of the AR at approximately 40°S–19°E in early June 2021 (location 1). Over the following three months, until early September 2021, the ring propagated westward, exiting the Agulhas Current Retroflection region (between 16–20°E; location 2) (Lutjeharms and Van Ballegooyen, 1988). When the AR reached near (39.1°S, 11.1°E) (location 3), it shifted northward to near 35.5°S in mid-October 2021 (location 4). Subsequently, after resuming a westward trajectory, the AR reached the hydrographic stations area (red dots) in mid-January 2022 (location 5). Over the next four months, until mid-April 2022, the ring remained confined within the region bounded by 37.7–36.4°S and 3.5–4.5°E (location 6). Finally, by the end of August 2022, the eddy migrated northwestward, reaching 34.4°S (location 7).

The translation speed of the AR, computed from the trajectory of the eddy center using daily altimetry maps, is shown in Figure 5. A Butterworth low-pass filter of a 30 days period was applied to reduce high-frequency fluctuations. Between 1 June 2021 and 24 August 2022, the AR exhibited a mean translation speed close to 11 cm/s. Shortly after detaching from the Agulhas Current Retroflection, the AR accelerated to 19 cm/s on 30 July 2021. The AR alternated between episodes of quasi-stationary motion around specific locations (e.g., positions 2, 3, and 4 in Figure 4) and phases of near linear propagation. For instance, on 19 August 2021 the AR drifted near (39.5°S, 14.4°E) at 13 cm/s (Figures 4, 5). During its northwestward

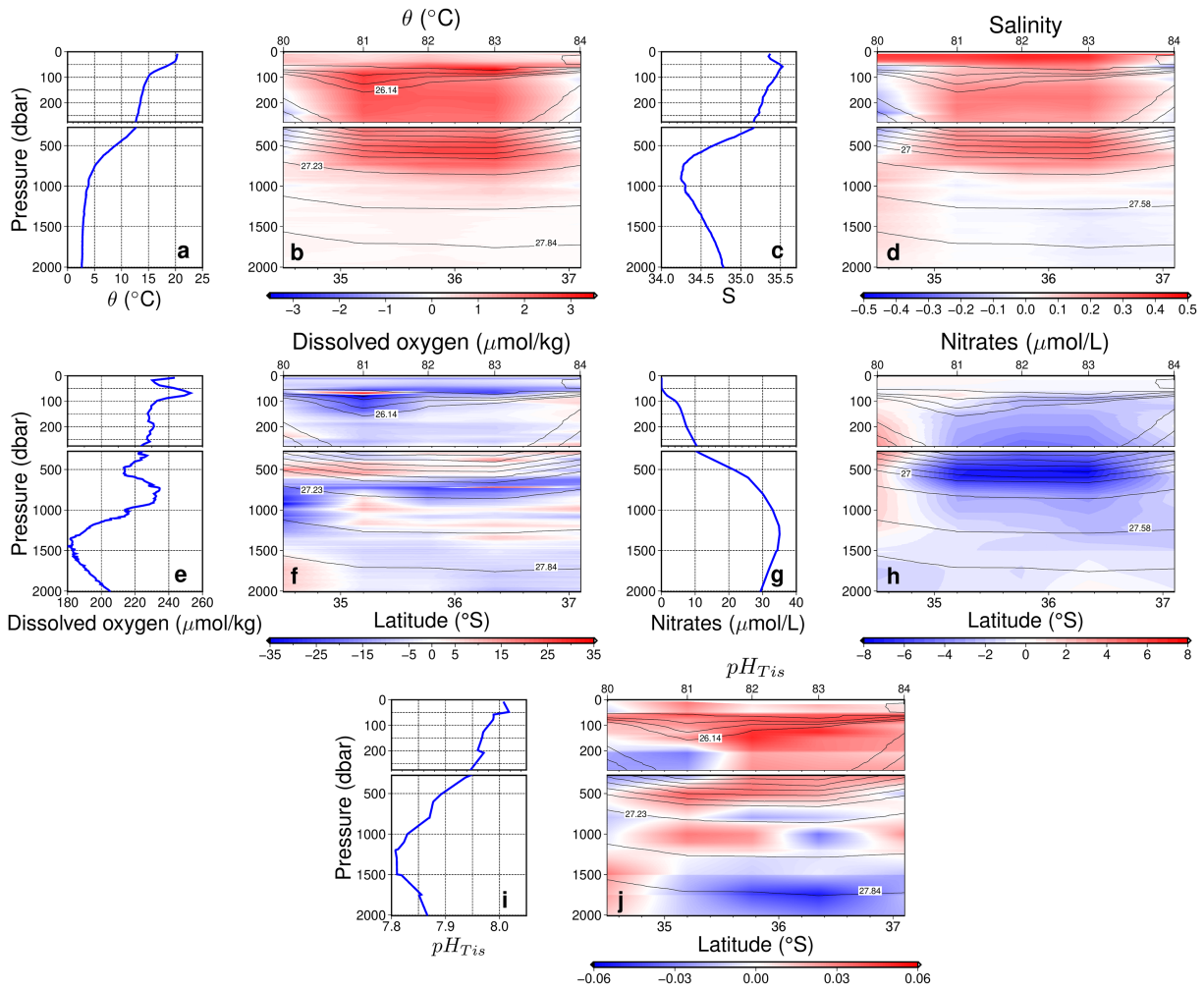

FIGURE 3
Vertical profiles for the reference state (defined as the mean of the stations from T1-AS) and vertical sections of anomalies along the transect across the AR (T2-AR). **(a, b)** Potential temperature; **(c, d)** salinity; **(e, f)** dissolved oxygen; **(g, h)** nitrates; and **(I, j)** pH_{Tis}. Anomalies are calculated as the difference between properties inside the ring and those in the reference state. A zoom of the upper 275 dbar is shown. Black lines in the vertical sections represent neutral density contours. Tick marks at the top of each vertical section indicate the position of each hydrographic station. The AR exhibits strong anomalies gradually weaken with distance.

drift (between positions 2 and 4 in Figure 4), the AR reached a maximum translation speed of 24 cm/s on 18 October 2021 (Figure 5), likely driven by the northward Benguela Current. Over the subsequent months, the translation speed ranged between 8 and 13 cm/s until 7 March 2022, when the AR reached the hydrographic stations. Afterward, its speed decreased to 5–10 cm/s (Figure 5).

3.3 Eddy circulation

During the hydrographic survey conducted on 6–7 March 2022, the AR was identified by a maximum SLA of about 38 cm (Figure 6a). Figure 6 presents the SLA maps along with the SADCP velocity field vectors (black arrows) during the survey.

On the northern flank of the ring, the velocity was directed northwestward, with a maximum of 57 cm/s at 35 m and 30 cm/s at 715 m. On the southern flank, the velocity shifted to the northeast, with a maximum of 52 cm/s at 35 m and 22 cm/s at 715 m (Figure 6). The eddy center, located at 36.05°S, was marked by minimum SADCP velocities of 2 cm/s at 35 m and 3 cm/s at 715 m (Figures 6a, b). The decrease in velocity magnitude with depth is consistent with the baroclinic structure of the ring.

Some localized departures of the velocity vectors from the SLA contours, likely reflect a combination of temporal mismatch between the satellite-derived SLA field (7 March 2022) and the shipboard measurements collected over 6–7 March, as well as ageostrophic contributions (e.g., curvature effects and transient adjustments) that are not captured by the instantaneous altimetric field. Overall, however, the velocity field is largely aligned with the SLA gradients and consistent with the anticyclonic circulation of the AR.

The northernmost portion of the T2-AR transect (≈80 km) was excluded from the dynamical and energetic analysis presented below. This segment is influenced by the interaction between the AR and a neighboring cyclonic structure located to the north, which induces a local intensification of the velocity field and distorts the characteristic circulation of the ring. As a result, velocities in this section are not representative of the intrinsic structure of the Agulhas Ring, and their inclusion would bias the estimates of its dynamical and energetic properties.

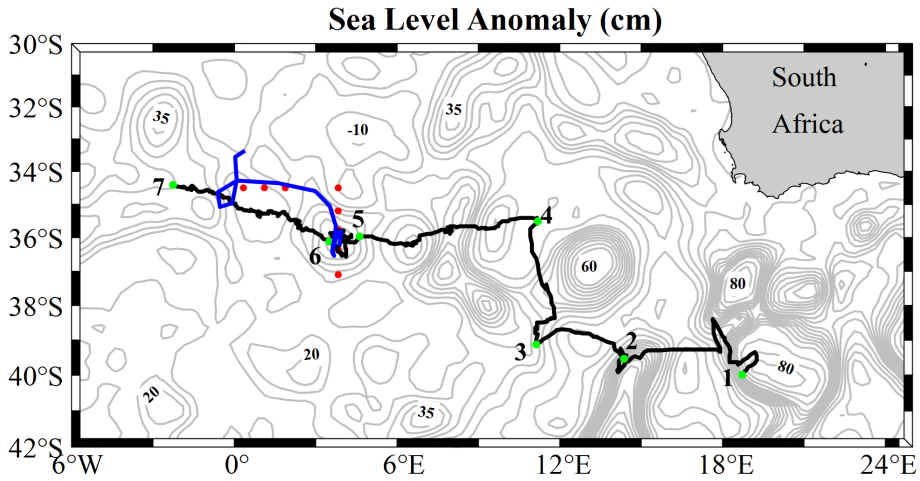

FIGURE 4
Altimetry map of SLA (cm) on 7 March 2022. The red dots represent the position of the hydrographic stations for T1-AS and T2-AR. The black bold line represents the path of the ring center from 1 June 2021 to 31 August 2022, as deduced from the SLA maximum. The green dots represent the locations of the Agulhas Ring center at different dates: (1) 1 June 2021, (2) 19 August 2021, (3) 09 September 2021, (4) 21 October 2022, (5) 17 January 2022, (6) 14 April 2022, and (7) 31 August 2022. The blue line represents the SOCCOM trajectory during its first 17 cycles, from 7 March 2022 to 18 August 2022 (the time period when the drifter remained within the AR).

The SADCP vertical section of the cross-transect velocity (Figure 6) exhibits the structure associated with an anticyclonic eddy, with eastward flow on the northern flank and westward on the southern flank. The eddy center (0 km) is marked by a transition zone of weak velocities, separating these opposite flows. The persistence of significant velocities below 400–500 m indicates that the eddy extends well into the thermocline, consistent with a vertically coherent structure characteristic of Agulhas rings.

3.4 Eddy trapping capacity

Assuming that the AR can be approximated, to first order, as a coherent rotating structure with predominantly azimuthal flow and comparatively radial and vertical motions, the radial momentum balance can be described within a cyclogeostrophic framework (Simpson et al., 1984; Sangrà et al., 2007; Valencia et al., 2025). Under this idealized assumption, the centripetal acceleration associated with the curved trajectories is balanced by the combined action of the Coriolis force and the radial pressure gradient, so that the radial force balance at all depths can be written as:

$$-\frac{c_\theta^2}{r} = fc_\theta - \frac{1}{\rho_0}\frac{\partial p}{\partial r} \quad (1)$$

where c_θ is the azimuthal velocity, f is the Coriolis parameter, r is the radius, ρ_0 is the seawater density, and p is the pressure of the AR. Formulation of Equation 1 highlights that, when curvature effects become significant, part of the departure from geostrophic balance arises from the need to sustain circular motion through centripetal acceleration.

To assess the importance of the curvature in the momentum balance, we estimated the nondimensional Rossby number as $Ro = c_\theta/(fr)$. A threshold of $Ro \geq 0.1$ is commonly used to identify conditions under which curvature-induced centripetal acceleration becomes non-negligible in the momentum balance (Penven et al., 2014; Valencia et al., 2025). Because the T2-AR transect was oriented nearly perpendicular to the mean circulation of the eddy, the azimuthal velocity component c_θ can be approximated to the cross-transect velocity shown (Figure 7). Accordingly, this velocity component was adopted in the estimation of Ro, assuming $u \approx c_\theta$.

The calculated distribution of Ro reveals values >0.1 within the upper 150 m. Peak values (>0.3), are obtained at 300 m depth, and between 450 and 750 m. This indicates that curvature effects play a significant role in the momentum balance of the AR, particularly at radial distances $r \leq 20$ km. The elevated values of Ro suggest the presence of compensating ageostrophic velocities that contribute to sustaining the anticyclonic circulation.

To characterize the rotational structure of the AR, we examined the radial patterns and vertical variability of the azimuthal velocity. This integrated analysis offers a detailed description of the eddy's

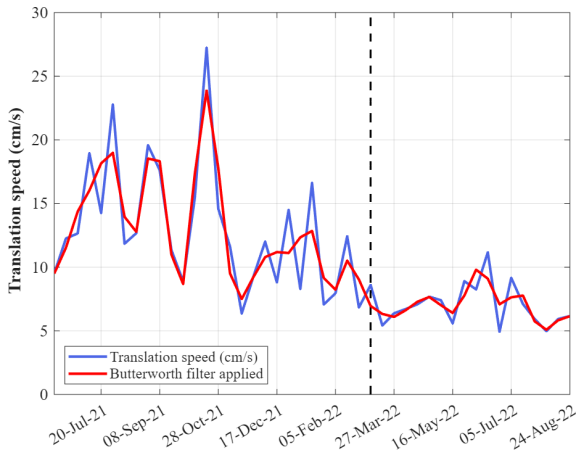

FIGURE 5
Temporal evolution of the 10-day average translation speed (cm/s) as inferred from altimetry data from 1 June 2021 to 31 August 2022 (blue line), and after applying a Butterworth filter to reduce high frequencies (red line). The dashed line represents the date of the SOCCOM first cycle (7 March 2022).

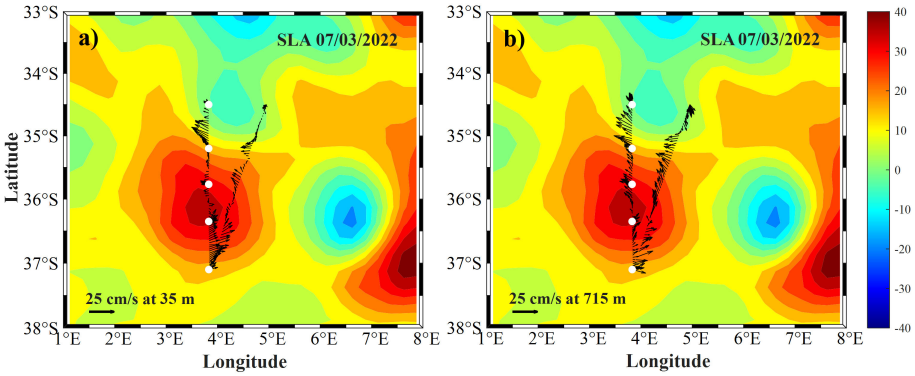

FIGURE 6
Surface SLA (cm) on 7 March 2022 (date of the first SOCCOM cycle) with contours every 5 cm. The black arrows represent the raw velocity field (cm/s) measured by the SADCP 75 kHz at **(a)** 35 m and **(b)** 715 m. The 35 m level corresponds to the shallowest depth with continuous spatial coverage along the ship track, avoiding near-surface data gaps, while 715 m represents the deepest level with reliable velocity measurements during the survey. White dots represent each of the hydrographic stations in T2-AR (80-84).

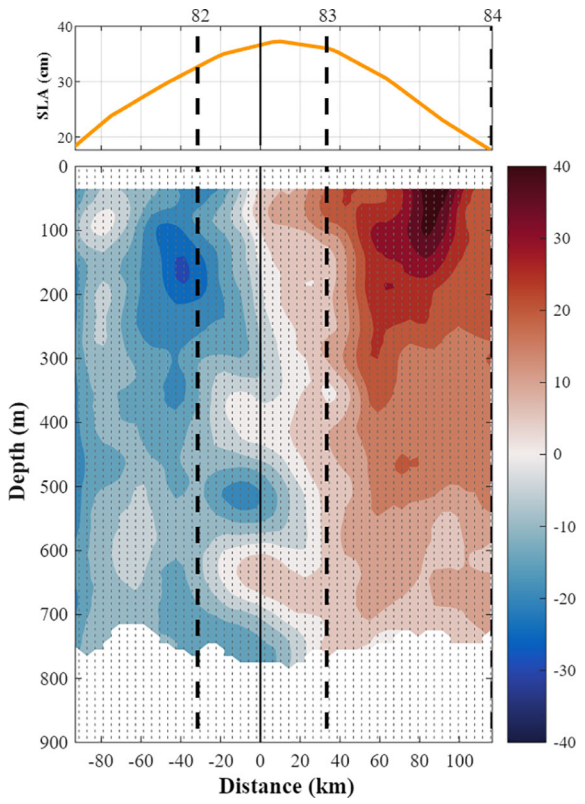

FIGURE 7
Vertical section of gridded cross-transect velocity (u component) measured by the SADCP along the meridional transect across the Agulhas Ring. Negative values indicate westward flow, while positive values indicate eastward flow. Contours are plotted every 5 cm/s. Black-dashed vertical lines mark the positions of the hydrographic stations (stations 82, 83, and 84), and the solid black line indicates the location of the eddy center (36.05°S). Gray-dot lines indicate the position of raw SADCP profiles. On top of the vertical section, SLA at each position is shown. The section reveals the characteristic velocity structure associated with the anticyclonic circulation of the ring.

internal dynamics, allowing both vertical consistency and radial changes in structure to be resolved.

Figure 8 shows radial distributions of c_θ for different depths. At each depth, the observed velocity field was fitted using a least-squares linear relationship of the form $c_\theta = \omega_\theta r$ to evaluate the extent to which the eddy core behaves as a solid-body rotation. In this expression, ω_θ represents the angular velocity, and the condition $c_\theta = 0$ at $r = 0$ was enforced. The fitting procedure was repeated progressively over expanding radial intervals, and the core radius was identified as the distance at which the correlation coefficient (r_{xy}) between the modeled and observed velocities reached the maximum value.

The radial structure of the azimuthal velocity reveals the presence of a coherent solid-body rotating core (Figure 8). At 85 m (Figure 8a), the azimuthal velocity increases approximately linearly with radius from the center up to ≈42 km, consistent with a solid-body rotation regime ($c_\theta \propto r$). Beyond this radius, the velocity gradually decreases toward the outer edge of the structure. A similar pattern is observed at 135 m (Figure 8b), where the solid-body region extends to ~38 km, followed by a velocity decline.

The vertical distribution of the rotation frequency ω_θ (Figure 8c) shows a clear decrease with depth. In the upper layers (approximately 40–80 m), ω_θ reaches values higher than 6×10^{-6} s^{-1}, corresponding to rotation periods of approximately 11–12 days. Between roughly 80 and 120 m depth, the profile shows a relative decrease in rotation frequency (and therefore longer rotation periods), followed by a renewed increase at intermediate depths (approximately 140–220 m), where the highest frequencies approach 7×10^{-6} s^{-1} and corresponding to periods close to 10 days. Below this level, the angular velocity decreases steadily, reaching values near 2.5-3 $\times 10^{-6}$ s^{-1} between 250 and 350 m (periods of 25–29 days). This vertical structure suggests that the eddy core is not vertically homogeneous but instead composed of layers with progressively slower rotation, indicating partial decoupling between upper and deeper levels. Overall, these results support the presence of a well-defined core with a core radius $R_c \approx 38 \pm 9$ km.

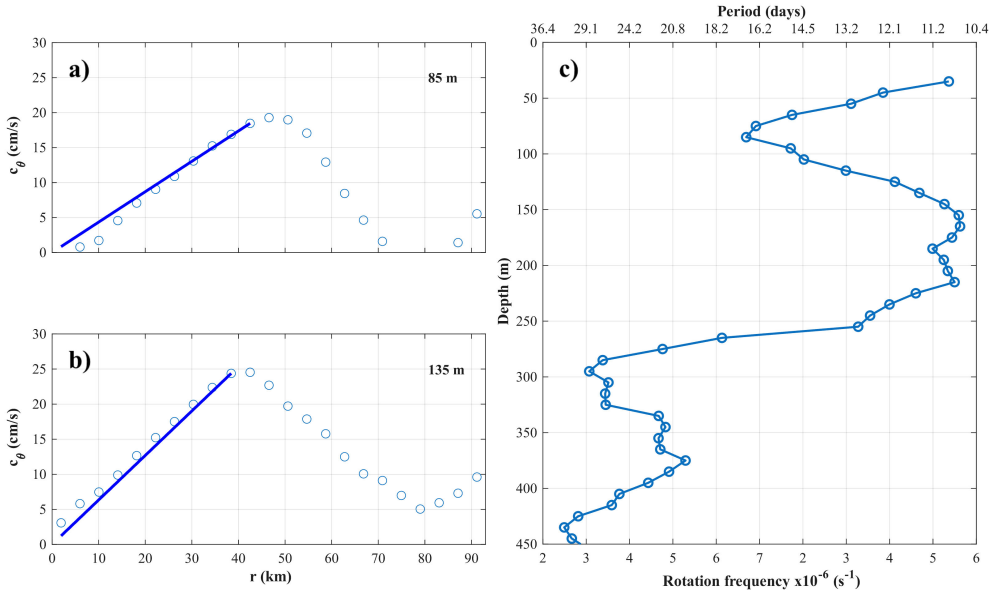

FIGURE 8
Radial profiles of azimuthal velocity (c_θ) at selected depths: **(a)** 35 m and **(b)** 65 m. Blue circles correspond to the observed data, while solid blue lines represent the linear regression fit using $c_\theta = \omega_\theta r$, with $c_\theta = 0$ at $r = 0$. The slope of the regression (ω_θ) is perpendicular to the angular velocity of the eddy. **(c)** Depth-wise variation of solid-body core's rotation frequency (ω_θ) and its corresponding period.

The persistence of property anomalies transported by the AR requires that water masses remain trapped inside the eddy, preventing exchange with surrounding waters (Barceló-Llull et al., 2017; Chaigneau et al., 2011; Flierl, 1981; Van Aken et al., 2003). Flierl (1981) introduced the non-dimensional parameter $\varepsilon = U/c$, defined as the ratio of a characteristic rotational velocity (U) to the translation speed c, which determines whether a trapped volume exists, its extent, and the intensity of the resulting disturbance (McCartney and Woodgate-Jones, 1991). For $\varepsilon < 1$, no water is trapped within the ring; $\varepsilon \approx 1$ indicates the presence of a stagnation zone; and $\varepsilon > 1$ implies nonlinear dynamics, with the trapped core maintaining coherence during propagation (Chaigneau et al., 2011; Flierl, 1981; McCartney and Woodgate-Jones, 1991).

Assuming a vertically uniform translation speed, Figure 9 compares depth-resolved estimates of characteristic rotational velocity with three representative translation speeds, computed as temporal averages over ±3.5 days, ± 7 days, and ±15 days around the sampling date. The rotational velocity is estimated using four complementary approaches: (i) the maximum absolute tangential velocity at each depth, $U_{max} = \max(|c_\theta|)$; (ii) the velocity at the radius of maximum velocity (RMV), obtained from the gridded velocity field and extracted as a vertical profile (U_{rmv}); (iii) the maximum absolute tangential velocity within the eddy core, $U_{maxCore} = max(\langle|c_\theta|\rangle_{\text{core}})$; and (iv) a section-based estimate derived from the zonal velocity along the transect, $U_{mean} = (|u_{\min}| + |u_{\max}|)/2$, assuming that the section crosses the eddy center. The intersection between the rotational velocity profiles and the prescribed translation speeds provides an estimate of the trapping depth, defined as the depth above which $\varepsilon \geq 1$, indicating that rotational velocities exceed or match the translation speed and fluid parcels remain dynamically trapped within the eddy.

A maximum in rotational velocities is observed in the upper layers, with a relative peak around 165 m depth. Below this maximum, velocities decrease sharply down to about 275 m. At greater depths, the decay becomes more gradual, extending to nearly 800 m. As shown in Figure 9, below approximately 445 m the $U_{maxCore}$ velocity approaches the magnitude of the translational speed. This suggests that at such depths, the eddy capacity to trap fluid parcels is weak. Same happens for U_{mean}, which indicates trapping capacity up to 595 m. The rest of characteristic rotational velocities indicate that the eddy maintains a coherent trapped core over a substantial portion of the water column (715 m), enabling the retention and transport of water masses along its trajectory.

3.5 Heat, salt and energy content

Following the method introduced by Joyce et al. (1981) and later used by Chaigneau et al. (2011); Laxenaire et al. (2019) and Valencia et al. (2025), we have computed the available heat and salt content anomalies (AHA and ASA, respectively) in the AR as:

$$AHA = \int_z^0 \int_0^{R_c} \rho c_p \theta' (2\pi r) dr dz \tag{2}$$

$$ASA = 0.001 \int_z^0 \int_0^{R_c} \rho S' (2\pi r) dr dz \tag{3}$$

where c_p is the specific heat capacity (J kg^{-1} °C^{-1}) computed from the hydrographic data, and θ' and S' are the potential temperature and salinity anomalies, respectively. AHA (Equation 2) and ASA (Equation 3) were integrated radially from the ring center to the edge of the ring core (R_c = 38 km, as described in Section 3.4), assuming the eddy volume to be cylindrical, and subsequently

10.3389/fmars.2026.1764162

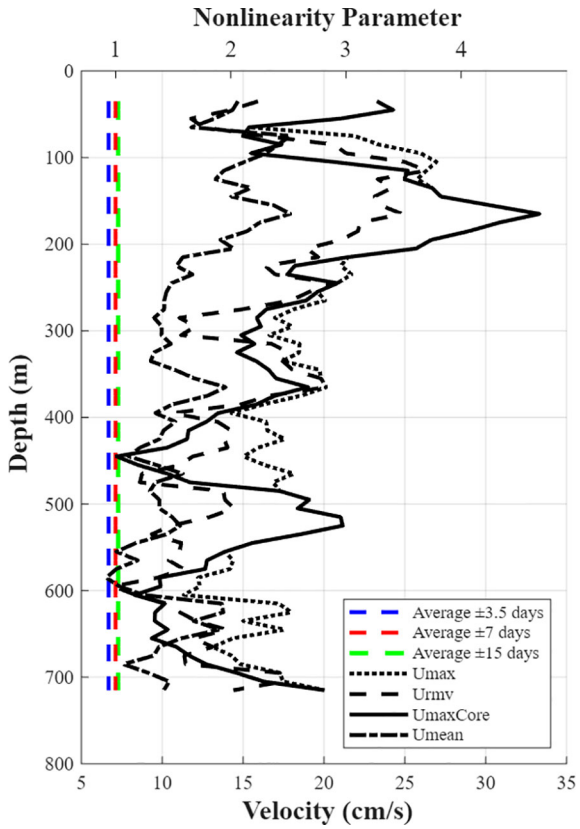

FIGURE 9
Vertical profiles of characteristic rotational velocities of the AR compared with representative translational speeds. Colored dashed lines indicate the translational speed, assumed vertically uniform, computed as temporal averages over ±3.5 days (blue), ± 7 days (red), ± 15 days (green) around the sampling date. Black curves represent different estimates of the rotational velocity: maximum tangential velocity (dotted), velocity at the radius of maximum velocity (dashed), maximum velocity within the eddy core (solid), and a section-based estimate derived from zonal velocities (dash-dot). The comparison between rotational and translational velocities provides an estimate of the trapping depth, defined as the depth range where the nonlinearity parameter $\varepsilon = U/c \geq 1$, indicating that the eddy is capable of trapping and transporting fluid parcels.

integrated vertically over the ring's vertical extent, defined here as the trapping depth of the eddy (z_1 = 445 m and z_2 = 595 m). This choice reflects the fact that thermohaline anomalies are primarily associated with the coherent, trapped core of the eddy, where water mass properties are preserved and less affected by lateral mixing. In Equation 3, the factor 10^{-3} converts salinity to a salinity fraction (kg of salt per kg of seawater).

For the AR, the integration to 445 m yields an AHA of 3.4 × 10^{19} J and an ASA of 1.1 × 10^{12} kg. Extending the vertical integration to 595 m increases these values to 4.9 × 10^{19} J and 1.5 × 10^{12} kg, respectively. This represents an increase of approximately 44% in AHA and 42% in ASA, highlighting the significant contribution of the deeper layers to the total thermohaline content of the eddy. These results underscore the importance of accurately constraining the trapping depth when quantifying the heat and salt anomalies associated with Agulhas rings.

The associated AHA (in Petawatts, 1 PW = 10^{15} W) and ASA (in Sverdrups, 1 Sv = 10^9 kg/s) transports were computed by multiplying these anomalies by the translation speed and dividing by the ring core diameter, following the approach of different authors (Doglioli et al., 2007; Laxenaire et al., 2019; Olson and Evans, 1986). Considering integrations down to 445 m and 595 m, and using the R_c = 38 km together with the average translational speed in March 2022 (6.9 cm/s), the instantaneous transports associated with the AR core crossing an imaginary section range from 0.03 to 0.04 PW for AHA and from 9.4 × 10^{-4} Sv to 1.0 × 10^{-3} Sv for ASA.

It is important to note, however, that these estimates are not directly comparable to most previous studies, which typically assess the mean impact of Agulhas Rings by dividing their heat and salt content by the number of seconds in one year (Garzoli et al., 1999; Laxenaire et al., 2019; Van Ballegooyen et al., 1994). Using this annualized approach, the corresponding AHA and ASA transports for the AR range from 0.001 to 0.002 PW and from 3.3 × 10^{-5} to 4.7 × 10^{-5} Sv, respectively. Finally, we computed the available potential energy (APE) and kinetic energy (KE) following the method proposed by Hebert (1988) and later applied by Tokos and Rossby (1991); Rae et al. (1996); Sangrà et al. (2005); Barceló-Llull et al. (2017) and Valencia et al. (2025):

$$APE = 0.5\rho_r \int_z^0 \int_0^R N_r^2 \delta^2 (2\pi r) dr dz \quad (4)$$

$$KE = 0.5\rho_r \int_z^0 \int_0^R |u_h|^2 (2\pi r) dr dz \quad (5)$$

where ρ_r and N_r are the density and Brunt–Väisälä frequency of the reference state, respectively; δ is the vertical displacement of the isopycnals within the AR relative to the reference state; and $u_h = u^2 + v^2$ is the squared horizontal velocity magnitude, with u and v representing the zonal and meridional velocity components from the SADCP measurements. The reference state was defined as the mean of stations 75, 76, and 77. The integrations of Equations 4 and 5 were performed from the surface to the vertical extent of the AR (z_1 = 445 m and z_2 = 595 m) and radially from the center to the core ring radius (R_c = 38 km) and to the radius of maximum azimuthal velocity (R_{max}= 86 km, Figure 6). The broader integration domain allows capturing the dynamical extent of the eddy, including its energetic outer circulation, which may extend beyond the strictly defined core.

At z_1 = 445 m, APE increased from 1.9 × 10^{15} J within R_c to 6.7 × 10^{15} J within R_{max}, while KE rose from 6.0 × 10^{13} J to 5.7 × 10^{14} J over the same radial range. Similarly, at (z_2 = 595 m, APE ranged from 2.1 × 10^{15} J (R_c) to 7.4 × 10^{15} J (R_{max}), and KE from 7.4 × 10^{13} J to 6.3 × 10^{14} J. In all cases, APE clearly exceeded KE, with differences of approximately two orders of magnitude at R_c and decreasing toward R_{max}, indicating a relative increase in the contribution of kinetic energy as larger portions of the eddy are included. The consistency of these estimates across both trapping depths suggests that the bulk energetics are robust to moderate variations in the vertical integration limit, while the systematic increase in both APE and KE with radius reflects the growing contribution of the outer eddy structure. This predominance of APE over KE is consistent with the typical energetic signature of coherent mesoscale eddies and supports the interpretation of the structure as a mature and dynamically stable feature.

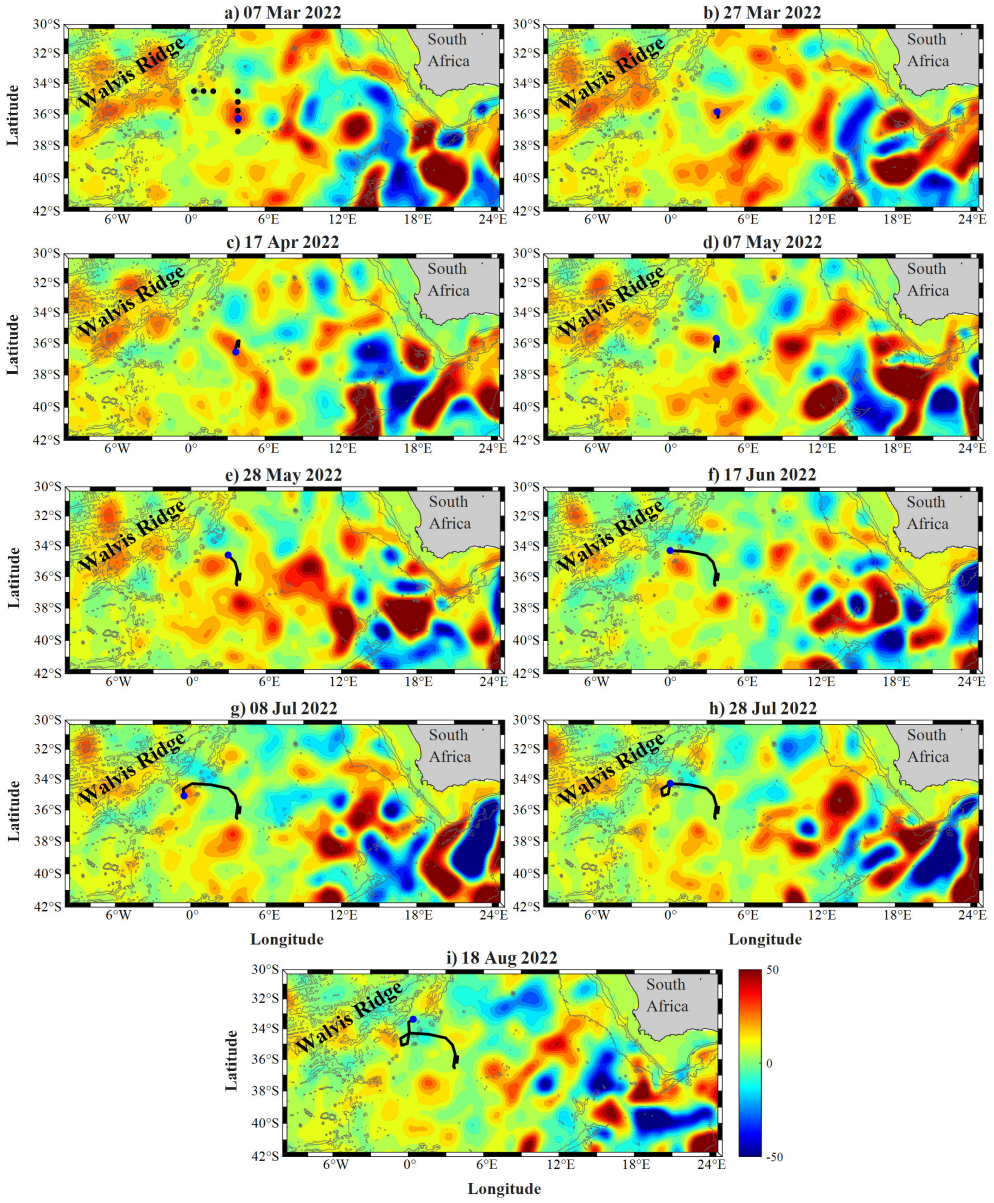

FIGURE 10
Daily SLA (cm) images from 7 March 2022 to 18 August 2022, approximately every 20 days. Each map presents the ring's trajectory since 7 March (black line) and the SOCCOM drifter location for the corresponding day (blue point). The gray lines represent the bathymetric contours corresponding to depths of 0, 500, 1000, 2000, and 4000 m. The sequence highlights the progressive deformation of the ring, including the emergence of a secondary SLA maxima in April-May 2022, indicative of the fragmentation as the ring approaches Walvis Ridge.

4 SOCCOM trajectory and measurements

On 6 March 2022, a SOCCOM profiler was deployed at the center of the AR, identified as a maximum SLA of 38 cm associated with the surface layer dome. Figure 10 shows a sequence of daily altimetry maps, approximately every 20 days, from the start of the first SOCCOM cycle (7 March 2022) until 5 months later, when the profiler exited the AR in August 2022.

At the time of deployment, the AR was centered near (36°S, 4°E) (Figure 10a). Over the following 40 days, the ring core remained close to the hydrographic station area, drifting slightly northwestward (Figures 4, 10b, c), while the SOCCOM float remained within the ring and completed five cycles. On 7 May 2022, SLA maps show the profiler positioned at the edge of the AR (Figure 10d). Between 28 May and 17 June 2022 (Figures 10e, f), the SOCCOM float stayed along the ring boundary for about 40 days, collecting data from the periphery while SLA remained near 30 cm. In July 2022, the profiler looped around the ring center (Figures 10g, h), and by mid-August 2022, when SLA had weakened to < 25 cm, it exited the AR (Figure 10i).

To quantitatively distinguish intrinsic temporal evolution from spatial sampling effects, we computed the normalized radial position of the float within the AR, defined as the ratio between the distance from SLA-derived ring center and the corresponding time-varying eddy radius ($R_n(t) = r(t)/R_{eddy}(t)$; Figure 11). Values of R_n <

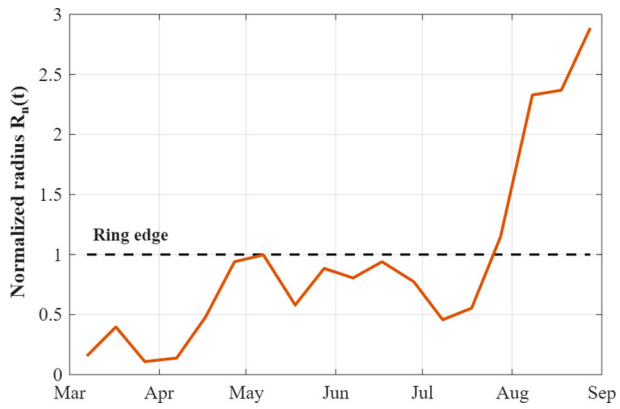

FIGURE 11
Time series from 2022 of the normalized radial position R_n (t) of the SOCCOM float within the Agulhas Ring, defined as the ratio between the float – center distance and the SLA-derived ring radius. The dashed line (R_n = 1) indicates the ring edge. Values below 1 correspond to sampling inside the ring, and values above 1 indicate that the float was outside the ring.

1 indicate sampling inside the ring, whereas $R_n > 1$ denotes that the float was outside the eddy. From early March to mid-April, the float remained within the inner core ($R_n < 0.5$). Between late April and June, it occupied intermediate to peripheral positions ($0.6 < R_n < 1$), briefly returning toward the interior in early July. After July, R_n exceeded 1, marking the float's exit from the AR.

Figure 12 presents selected SOCCOM profiles corresponding to different radial positions within the AR: at deployment, inside the ring, near the edge, and outside the AR. The time evolution of vertical profiles of potential temperature, salinity, oxygen, nitrate, and pH_{Tis} reveals a transition from AR-modified waters to surrounding South Atlantic waters.

Above 100 dbar, the initial SOCCOM profiles near the ring center (7 March and 7 April 2022) show warmer potential temperatures (20.6°C and 19.7°C, respectively; Figure 12a), higher salinity (35.8; Figure 12b), and lower oxygen concentrations (226 µmol/kg; Figure 12c) as compared to the profiles collected after the profiler left the AR on 18 August 2022 (16.1°C, 35.7, and 238 µmol/kg, respectively). Figure 12a and b further illustrate the progressive

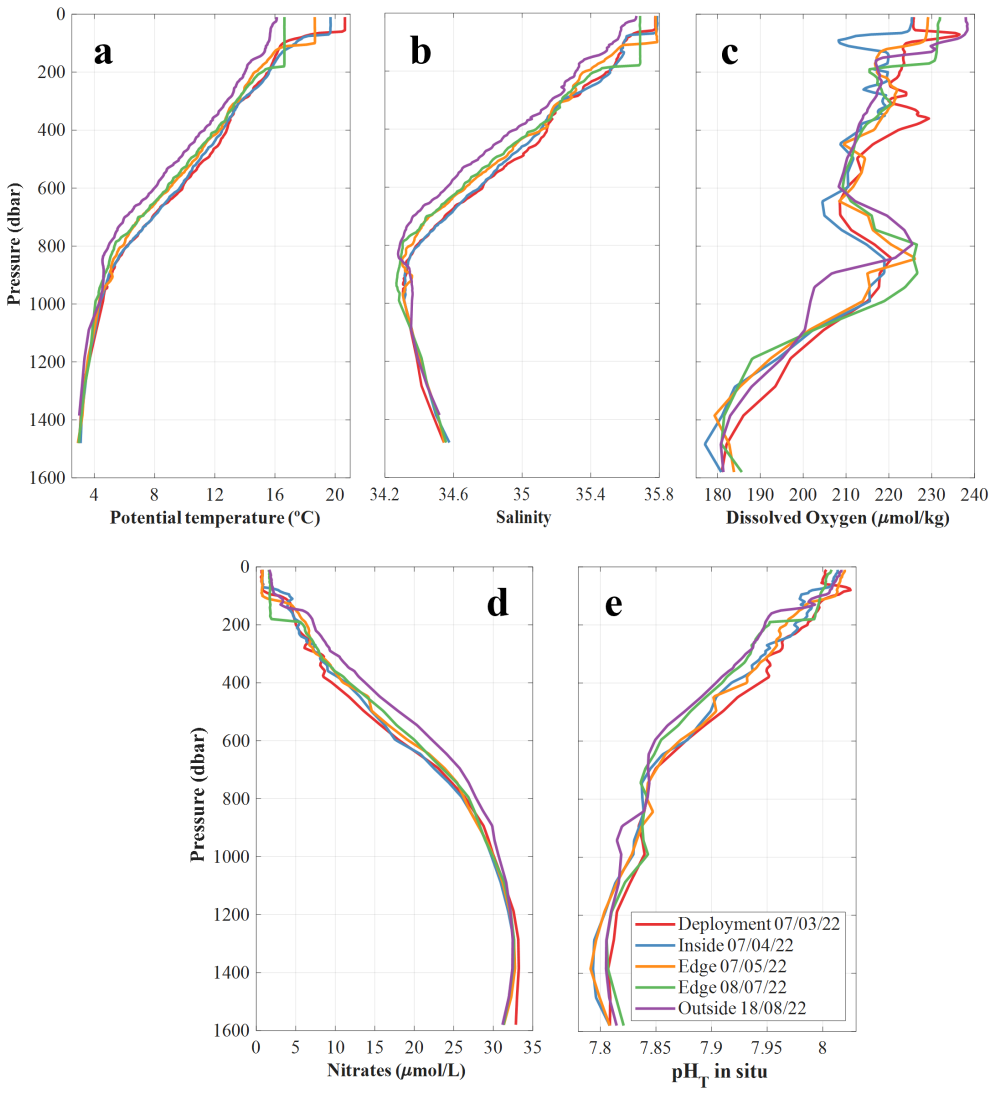

FIGURE 12
Vertical profiles of **(a)** potential temperature, **(b)** salinity, **(c)** dissolved oxygen, **(d)** nitrate, and **(e)** pH_{Tis} as measured by the SOCCOM drifter approximately every month between the deployment date and the time the drifter left the AR. Only selected profiles related to changes in the radial position of the SOCCOM within the AR are shown (see legend).

deepening of the mixed layer within the AR, from about 60 to nearly 180 dbar, forming a homogeneous upper layer in the inner-ring trapped waters. Here, the mixed-layer depth (MLD) is defined using a potential density criterion of $\Delta\sigma_\theta$ = 0.03 kg/m³ relative to 10 dbar (de Boyer Montégut et al., 2004). Importantly, the mixed-layer deepening observed between March and early April occurred while the float remained within the inner core (R_n<0.5, Figure 11), indicating *in situ* modification of the trapped waters rather than radial sampling artifact. In contrast, no distinct MLD is observed in profiles outside the eddy.

Within the eddy, below the MLD, clear signatures of biological activity are observed. Dissolved oxygen concentrations decrease to values below 200 µmol/kg, nitrate concentrations increase (up to ~3 µmol/L), and pH values are lower compared to the surrounding profiles. Together, these patterns are consistent with active remineralization processes occurring within the eddy.

On 7 March 2022, nitrate concentrations in surface waters were generally low (1–2 µmol/L; Figure 12d), with a nitracline near 75 dbar. As the profiler drifted out of the AR, the nitracline progressively deepened (Figure 12d), tracking the concurrent deepening of the thermocline and pycnocline (Figures 12a, b). This transition largely reflects coincidences with the float's migration toward the ring periphery (R_n > 0.6, Figure 11), suggesting that part of the apparent temporal evolution reflects radial gradients within the AR structure. This trend reflects that South Atlantic waters are comparatively nutrient-rich relative to AR waters. Differences in potential temperature and salinity between AR and the surrounding waters persist down to some 850 dbar (Figures 12a, b). Meanwhile, AR profiles show pH_{Tis} systematically higher values than South Atlantic waters, with differences of up to 0.04 at 400 dbar (Figure 12e).

Between 150 and 600 dbar, the AR is characterized by higher oxygen concentrations relative to surrounding waters, with mean differences of about 10 µmol/kg (Figure 12c). At the AAIW level, the DOM appears deeper and weaker within the AR (some 220 µmol/kg at 850 dbar) than outside (> 225 µmol/kg at 800 dbar), reflecting both the deepening of isopycnals and the regional prominence of AAIW in the South Atlantic (Figure 12c). After late July, when R_n exceeded 1, the vertical structure rapidly transitioned toward that of ambient South Atlantic waters, confirming that the late-stage hydrographic changes primarily reflect the float's detachment from the eddy rather than continued internal transformation.

5 Discussion and conclusions

This study provides a detailed characterization of the structure and trajectory of an Agulhas Ring (AR) sampled during the SAGA-34.5S cruise in March 2022 through hydrographic, thermosalinograph, SADCP, and SOCCOM profiler data, complemented with satellite altimetry.

Altimetry indicates that the AR was formed in early June 2021 in the ACR region (16-20°E) and propagated northwestward along the Agulhas Eddy Corridor (Garzoli and Gordon, 1996) before turning westward, following the pathways described by previous studies (Goni et al., 1997; Schouten et al., 2000). This trajectory highlights the possibility of Indian Ocean waters being trapped within the ring and transported into the South Atlantic Ocean, contributing to its thermohaline variability (Beal et al., 2011; Duncombe Rae, 1991; Pichevin et al., 1999).

The AR displayed a strong positive SLA signal (38 cm), consistent with long-lived rings (Gordon and Haxby, 1990; Guerra et al., 2018; Schouten et al., 2000). In contrast to its high surface-salinity signal, the surface thermal signature was less apparent. This absence of a thermal signal likely reflects the rapid erosion of surface temperature contrasts through heat exchange with the cooler atmosphere (Guerra et al., 2018; Mey et al., 1990; Olson et al., 1992). These results suggest that surface salinity provides a more persistent and reliable tracer of Agulhas rings than temperature, particularly in regions where atmospheric forcing efficiently dampens thermal anomalies.

Hydrographic data revealed that the density structure of the AR is characterized by isopycnal depressions down to 850 m, which is shallower than the typical 1500–2000 m depth reported for other ARs (Biastoch and Krauss, 1999). CTD data confirmed that the AR generated anomalies in both salinity and potential temperature above 850 dbar, with the 10°C thermocline displaced downward to some 600 m. Duncombe Rae (1991) reported an average thermocline depth of 650 ± 130 m for ARs, near the ring core. Within this layer, Indian Ocean waters were identifiable from the surface Agulhas Water to the intermediate Indian Central Water (ICW), while mixing between Red Sea Water (RSW) and Antarctic Intermediate Water (AAIW) was evident at greater depths. The presence of RSW is more explicitly identified in the θ–S diagram (Figure 2), where intermediate waters within the AR exhibit a clear salinity enrichment relative to the AAIW salinity minimum (<34.3), together with slightly elevated temperatures, consistent with the characteristic RSW signature described in previous studies (Casanova-Masjoan et al., 2017; Van Aken et al., 2003). The θ–S range between the salty RSW and fresher AAIW highlights strong mixing of Indian and Atlantic waters at these depths (Giulivi and Gordon, 2006).

Property anomaly distributions indicated a ring extent consistent with previously reported AR dimensions of 100–200 km (Biastoch et al., 2008; Casanova-Masjoan et al., 2017; Duncombe Rae, 1991; Laxenaire et al., 2019; Schouten et al., 2000). The ring core was characterized by warmer, saltier, more alkaline, and less oxygenated waters relative to the surrounding Atlantic. The maximum temperature (≈2.5°C) and salinity anomalies (≈0.4 psu) observed in the core are moderate compared to values reported for recently detached Agulhas Rings, which can reach up to ≈5°C and ~1 psu (Garzoli et al., 1999; Gordon et al., 1992; Lutjeharms, 2006, 2007). This attenuation is consistent with the estimated ≈9 months westward drift of the ring, during which partial mixing and equilibration with surrounding South Atlantic waters are expected. In this context, the persistence of relatively strong salinity anomalies compared to temperature reinforces that salinity anomalies decay more slowly and provide a more robust tracer of Indian Ocean water mass origin.

Nitrate anomalies further reflected the nitrogen-limited nature of the Agulhas system (Marshall et al., 2023; Voss et al., 2013). These biogeochemical anomalies are primarily consistent with the lateral advection of Indian Ocean waters trapped within the ring, which retain their original thermohaline and chemical signatures

during westward propagation. However, the observed variability in dissolved oxygen, nitrate and pH may also reflect the influence of *in situ* biological processes, such as remineralization and organic matter cycling within the eddy interior. SOCCOM profiles corroborated these anomalies, capturing their gradual weakening as the drifter exited the AR.

The normalized radial position analysis (Figure 11) provides additional context for interpreting the AR evolution. During the first 5 cycles after deployment, when the float remained within the inner core ($R_n < 0.5$), the observed deepening of the mixed layer and modest thermohaline changes indicate genuine *in situ* modification of the trapped waters.

The nearly 180 dbar-thick surface homogeneous layer observed within the ring core likely reflects not only seasonal surface mixing but also the upper expression of a warm-saline mode-water lens characteristic of Agulhas Rings. The weak vertical gradients in temperature and salinity within this layer, together with its persistence below the seasonally ventilated surface layer, suggest that it represents a combination of winter mixed-layer deepening and the vertically coherent core structure of the eddy. In contrast, much of the observed anomaly reduction coincided with the float's migration toward the ring periphery ($0.6 < R_n < 1$) and eventual exit ($R_n > 1$), indicating that part of the apparent temporal decay reflects the strong radial gradients that characterize Agulhas Rings rather than solely intrinsic dissipation.

It is worth noting that between 150 and 600 m, Indian waters inside the AR contained higher oxygen concentrations than South Atlantic waters (Figure 12c), reflecting the winter properties of central waters formed in the ACR region (Arhan et al., 1999). Importantly, the displacement of the deep oxygen maximum (DOM) to some 850 m (Figure 12c), deeper than in adjacent Atlantic waters, highlights the deepening and vertical adjustment of the AAIW layer induced by the eddy, consistent with previous studies (Schmid et al., 2003). Below 850 dbar, the SOCCOM profiles converged with ambient conditions, indicating that the AR signal was no longer detectable at intermediate depths.

After late July, once R_n exceeded 1, the rapid convergence of thermohaline and biogeochemical properties toward ambient South Atlantic conditions confirms that the eddy signal was no longer dynamically connected to the float, marking the effective end of coherent AR influence at the sampling location.

Dynamic signatures showed counterclockwise geostrophic circulation, with peak velocities of 24 and 35 cm/s near 60 dbar. These values are substantially lower than the peak velocities reported by Van Aken et al. (2003), which can exceed 100 cm/s for newly formed rings. However, the observed values are consistent with observations for more evolved structures of (Laxenaire et al., 2018, 2019). Velocity profiles revealed both baroclinic decay at the periphery and barotropic-like behavior near the core, suggesting a transition in dynamical regimes within the AR. In addition, the presence of localized counterflows and vertical shear near the eddy center suggests a dynamically complex structure, potentially associated with internal adjustment processes or baroclinic instability, as indicated by the SADCP observations (Figure 7).

The ring's translational evolution followed distinct phases: a rapid detachment and interaction with the Benguela Current (13–19 cm/s), acceleration westward (up to 24 cm/s), and gradual deceleration (5–10 cm/s) as it approached Walvis Ridge (34°S, 1°E). This decrease is also associated with the interaction with the Walvis Ridge by Byrne et al. (1995). Matano and Beier (2003) proposed that most ARs in the Cape Basin follow a narrow westward pathway before dissipating their energy into smaller eddies upon encountering the Walvis Ridge. In addition to topographic interactions, the observed weakening may reflect the natural spin-down of the eddy due to energy dissipation, as well as interactions with the surrounding flow field, including mesoscale variability. These processes can contribute to the gradual loss of coherence and kinetic energy. Our altimetry maps support this view: five months after its formation, upon reaching Walvis Ridge, the AR exhibited a gradual reduction in surface SLA together with deformation of the SLA core and the appearance of a secondary maxima (Figures 10c–e), consistent with fragmentation into smaller rings in April 2022.

The radial structure of the azimuthal velocity reveals a coherent solid-body rotating core with radius $R_c \approx 38 \pm 9$ km, characterized by a near-linear increase of velocity with radius and, consequently, an approximately uniform relative vorticity. This core structure weakens with depth, as evidenced by the decrease in angular velocity, indicating partial vertical decoupling between upper and deeper layers. Such vertical variability suggests that the eddy cannot be considered vertically homogeneous, but rather composed of layers with distinct dynamical characteristics (Tokos and Rossby, 1991; Valencia et al., 2025). In agreement with theoretical expectations (Flierl, 1981), the ratio of azimuthal to translation speed ($\varepsilon > 1$) confirms the presence of a dynamically coherent trapped core. Further, the trapping depth analysis indicates that this condition is satisfied down to at least 595 m.

Energy and transport diagnostics further underscore the significance of the observed AR. The estimated heat and salt anomalies (AHA ranging from 3.4×10^{19} to 4.9×10^{19} J and ASA from 1.1×10^{12} to 1.5×10^{12} kg) fall within the range of previous studies. Lower AHA values ($1.4\text{-}4.2 \times 10^{19}$ J) and ASA values ($1.2\text{-}3.8 \times 10^{12}$ kg) have been reported for rings in the eastern Cape Basin (McDonagh et al., 1999; Rae et al., 1996), while higher values ($1.0\text{-}2.5 \times 10^{20}$ J and $4.4\text{-}13.1 \times 10^{12}$ kg) are typically associated with younger or less dissipated rings near the ACR or further downstream (Laxenaire et al., 2019; Schmid et al., 2003; Van Ballegooyen et al., 1994). Given that the studied ring is located at 36°S, 3.8°E—between the ACR region (16–20°E) and the Walvis Ridge region (~34°S, 1°E)—its intermediate AHA and ASA values are consistent with a stage of partial equilibration during westward propagation.

The variability between estimates associated with different trapping depths (42-44%) highlights the sensitivity of thermohaline content to the vertical extent of the dynamically trapped core, while also indicating that a significant fraction of the anomaly is concentrated above 600 m.

Instantaneous transport estimates (0.03-0.04 PW and 9.4×10^{-4} to 1.0×10^{-3} Sv) are relatively large, reflecting strong signal associated with the eddy core crossing a section. However, when expressed as annualized contributions ($1\text{-}2 \times 10^{-3}$ PW and 3.3×10^{-5} to 4.7×10^{-5} Sv), the values fall below those reported for younger or more energetic rings (e.g. $2.3\text{-}7.5\times 10^{-3}$ PW and $1.4\text{-}4.2 \times 10^{-4}$ Sv in Van Ballegooyen et al., 1994; 8×10^{-3} PW and 3×10^{-4}

Sv in Laxenaire et al., 2019), reinforcing the interpretation of a dynamically evolving and partially dissipated structure.

Finally, the estimated APE and KE span a range depending on both radial and vertical integration limits, with APE between 1.9×10^{15} J and 7.44×10^{15} J and KE between 6.0×10^{13} J and 6.3×10^{14} J. The values agree with earlier studies of ARs (Clement and Gordon, 1995; Rae et al., 1996; McDonagh et al., 1999) and highlight the predominance of potential over kinetic energy. The resulting APE/KE ratio ranges from approximately 10 to more than 20, depending on the integration domain, which is consistent with previous estimates (e.g. APE/KE ratio between 2 and 10 in Rae et al., 1996; APE/KE ratio between 3 and 5 in McDonagh et al., 1999) and confirms that the eddy is strongly dominated by available potential energy.

The large APE-KE imbalance suggests susceptibility to baroclinic instability and eventual decay through energy conversion (from potential into kinetic), consistent with the fragmentation of ARs into smaller eddies (de Steur and van Leeuwen, 2009; Kang and Curchitser, 2015; Li et al., 2023; Matano and Beier, 2003). In this context, the observed fragmentation of the ring likely represents a stage in which part of this excess APE is released and converted into kinetic energy of smaller-scale structures, supporting the hypothesis that high-APE rings are more prone to instability and energy shedding. The large energy reservoirs associated with the observed AR further suggest that Agulhas Rings could play an important role in ocean mixing and the redistribution of heat, salt, and energy across ocean basins (Li et al., 2023; Van Ballegooyen et al., 1994).

Although this study focuses on a single Agulhas Ring, its main characteristics—including radius, SLA amplitude, thermohaline anomalies, and energetic structure—fall within the range reported for the broader Agulhas Ring population. The ring exhibits properties consistent with a mature structure located between the Agulhas Current Retroflection and the Walvis Ridge, suggesting that it is representative of a common evolutionary stage rather than an exceptional case. Therefore, while caution is required when generalizing from a single observation, the processes described here are likely relevant to a significant fraction of Agulhas Rings propagating across the Cape Basin.

Regarding question 1 in Introduction (How do the vertical structure and energetics of an Agulhas Ring evolve after detachment)?, our analysis shows that the vertical structure and energetics of the Agulhas Ring evolve significantly after detachment, with progressive weakening of thermohaline anomalies, reduction in rotational velocities, partial vertical decoupling, and a sustained dominance of available potential energy over kinetic energy. These changes reflect a transition from a newly formed to a mature and dynamically evolving eddy.

Regarding the second question (What does this evolution tell us about the ring's contribution to interocean exchange)?, this evolution implies that the contribution of Agulhas Rings to interocean exchange is not constant but depends on their life stage. Even in a partially equilibrated state, the ring retains sufficient thermohaline and energetic anomalies to contribute significantly to the transport of heat, salt, and water masses across the South Atlantic.

In summary, our results confirm that Agulhas Rings are not only efficient carriers of Indian Ocean waters into the South Atlantic but also dynamically active features with significant impacts on thermohaline structure, transport, and energetics. Their persistence and energetic content highlight their fundamental role in the Agulhas leakage system and in shaping variability across the South Atlantic Ocean.

Data availability statement

The datasets presented in this study can be found in online repositories. The names of the repository/repositories and accession number(s) can be found below: the drifter data were collected from SOCCOM project can be found at https://soccom.princeton.edu/observations/data-access. Satellite altimetry data it's available at https://data.marine.copernicus.eu/product/SEALEVEL_GLO_PHY_L4_NRT_008_046/description. The hydrographic data collected during the expedition of the Spanish Research Vessel Sarmiento de Gamboa at 34.5°S conducted in 2022 and as part of SAGA research project can be found at https://doi.org/10.1594/PANGAEA.972164, https://doi.org/10.1594/PANGAEA.972150, https://doi.org/10.1594/PANGAEA.972151, https://doi.org/10.1594/PANGAEA.971796, https://doi.org/10.1594/PANGAEA.972173, https://doi.org/10.1594/PANGAEA.972891.

Author contributions

MN-B: Methodology, Formal analysis, Data curation, Conceptualization, Visualization, Writing – original draft, Investigation, Writing – review & editing. CA: Writing – review & editing, Conceptualization, Methodology. JP: Funding acquisition, Project administration, Writing – review & editing, Conceptualization. MP-H: Project administration, Conceptualization, Funding acquisition, Writing – review & editing. PV-B: Writing – review & editing, Project administration, Funding acquisition. AH-G: Funding acquisition, Writing – review & editing, Project administration, Resources, Methodology, Conceptualization, Investigation, Supervision.

Funding

The author(s) declared that financial support was received for this work and/or its publication. This study has been supported by SAGA (RTI2018-100844-B-C31, RTI2018-100844-B-C32, and RTI2018-100844-B-C33) and SACO (PID2022-139403NB-C21 and PID2022-139403NB-C22) projects funded by the Ministerio de Ciencia, Innovación y Universidades of the Spanish Government, and European Regional Development Fund (ERDF) of the European Union. This work was conducted by MN-B as part of her work at IOCAG, in the doctoral program in Oceanography and Global Change. MN-B recognizes "Agencia Canaria de Investigación, Innovación y Sociedad de la Información (ACIISI) de la Consejería de Universidades, Ciencia e Innovación y Cultura" and "Fondo Social Europeo Plus (FSE+) Programa Operativo Integrado de Canarias 2021-2027, Eje 3 Tema Prioritario 74 (85%)" for grant program of "Apoyo al personal investigador en

formación" TESIS2024010016. JP also recognizes the institutional support of the Spanish Government through the Severo Ochoa Center of Excellence accreditation (CEX2019-000928-S).

Acknowledgments

MN-B also acknowledges the collaboration of Adrián Vega Morales, hired by the INVESTIGO program for the hiring of young people in research and innovation initiatives within the framework of the "Plan de Recuperación, Transformación y Resiliencia", financed by the European Union - "NEXT-GENERATION-EU".

Conflict of interest

The author(s) declared that this work was conducted in the absence of any commercial or financial relationships that could be construed as a potential conflict of interest.

Generative AI statement

The author(s) declared that generative AI was used in the creation of this manuscript. The author(s) acknowledge that generative AI tools contributed to the preparation of this manuscript. ChatGPT (GPT-5.1, OpenAI) was employed to support language refinement and improvements to clarity during writing. All content was subsequently reviewed, edited, and fully validated by the author(s) to ensure accuracy and integrity.

Any alternative text (alt text) provided alongside figures in this article has been generated by Frontiers with the support of artificial intelligence and reasonable efforts have been made to ensure accuracy, including review by the authors wherever possible. If you identify any issues, please contact us.

Publisher's note

All claims expressed in this article are solely those of the authors and do not necessarily represent those of their affiliated organizations, or those of the publisher, the editors and the reviewers. Any product that may be evaluated in this article, or claim that may be made by its manufacturer, is not guaranteed or endorsed by the publisher.

Supplementary material

The Supplementary Material for this article can be found online at: https://www.frontiersin.org/articles/10.3389/fmars.2026.1764162/full#supplementary-material.

References

Arhan, M., Mercier, H., and Lutjeharms, J. R. E. (1999). The disparate evolution of three Agulhas rings in the South Atlantic Ocean. *J. Geophys Res: Oceans* 104, 20987–21005. doi: 10.1029/1998JC900047

Arruda, W., Zharkov, V., Deremble, B., Nof, D., and Chassignet, E. (2014). A new model of current retroflection applied to the westward protrusion of the Agulhas Current. *J. Phys. Oceanogr.* 44, 3118–3138. doi: 10.1175/JPO-D-14-0054.1

Arumí-Planas, C., Pérez-Hernández, M. D., Pelegrí, J. L., Vélez-Belchí, P., Emelianov, M., Cainzos, V., et al. (2023). The South Atlantic circulation between 34.5°S, 24°S and above the Mid-Atlantic Ridge from an inverse box model. *J. Geophys Res: Oceans* 128, e2022JC019614. doi: 10.1029/2022JC019614

Barceló-Llull, B., Sangrà, P., Pallàs-Sanz, E., Barton, E. D., Estrada-Allis, S. N., Martínez-Marrero, A., et al. (2017). Anatomy of a subtropical intrathermocline eddy. *Deep Sea Res. Part. I: Oceanograph Res. Papers* 124, 126–139. doi: 10.1016/j.dsr.2017.03.012

Beal, L. M., De Ruijter, W. P. M., Biastoch, A., Zahn, R., Cronin, M., Hermes, J., et al. (2011). On the role of the Agulhas system in ocean circulation and climate. *Nature* 472, 429–436. doi: 10.1038/nature09983

Biastoch, A., and Krauss, W. (1999). The role of mesoscale eddies in the source regions of the Agulhas Current. *J. Phys. Oceanogr.* 29, 2303–2317. doi: 10.1175/1520-0485(1999)029<2303:TROMEI>2.0.CO;2

Biastoch, A., Lutjeharms, J. R. E., Böning, C. W., and Scheinert, M. (2008). Mesoscale perturbations control inter-ocean exchange south of Africa. *Geophys. Res. Lett.* 35(20). doi: 10.1029/2008GL035132

Byrne, D. A., Gordon, A. L., and Haxby, W. F. (1995). Agulhas eddies: A synoptic view using Geosat ERM data. *J. Phys. Oceanogr.* 25, 902–917. doi: 10.1175/1520-0485(1995)025<0902:AEASVU>2.0.CO;2

Casanova-Masjoan, M., Pelegrí, J. L., Sangrà, P., Martínez, A., Grisolía-Santos, D., Pérez-Hernández, M. D., et al. (2017). Characteristics and evolution of an Agulhas ring. *J. Geophys Res: Oceans* 122, 7049–7065. doi: 10.1002/2017JC012969

Chaigneau, A., Le Texier, M., Eldin, G., Grados, C., and Pizarro, O. (2011). Vertical structure of mesoscale eddies in the eastern South Pacific Ocean: A composite analysis from altimetry and Argo profiling floats. *J. Geophys Res: Oceans*. 116(C11). doi: 10.1029/2011JC007134

Clement, A. C., and Gordon, A. L. (1995). The absolute velocity field of Agulhas eddies and the Benguela Current. *J. Geophys Res: Oceans* 100, 22591–22601. doi: 10.1029/95JC02421

de Boyer Montégut, C., Madec, G., Fischer, A. S., Lazar, A., and Iudicone, D. (2004). Mixed layer depth over the global ocean: An examination of profile data and a profile-based climatology. *J. Geophys Res: Oceans* 109, 1–20. doi: 10.1029/2004JC002378

De Ruijter, W. P. M., Biastoch, A., Drijfhout, S. S., Lutjeharms, J. R. E., Matano, R. P., Pichevin, T., et al. (1999). Indian-Atlantic interocean exchange: Dynamics, estimation and impact. *J. Geophys Res: Oceans* 104, 20885–20910. doi: 10.1029/1998JC900099

de Steur, L., and van Leeuwen, P. J. (2009). The influence of bottom topography on the decay of modeled Agulhas rings. *Deep Sea Res. Part. I: Oceanograph Res. Papers* 56, 471–494. doi: 10.1016/j.dsr.2008.11.009

Doglioli, A. M., Blanke, B., Speich, S., and Lapeyre, G. (2007). Tracking coherent structures in a regional ocean model with wavelet analysis: Application to Cape Basin eddies. *J. Geophys Res: Oceans* 112(C5). doi: 10.1029/2006JC003952

Duncombe Rae, C. M. (1991). Agulhas retroflection rings in the South Atlantic Ocean: An overview. *South. Afr. J. Mar. Sci.* 11, 327–344. doi: 10.2989/025776191784287574

Elipot, S., and Beal, L. M. (2015). Characteristics, energetics, and origins of Agulhas Current meanders and their limited influence on ring shedding. *J. Phys. Oceanogr.* 45, 2294–2314. doi: 10.1175/JPO-D-14-0254.1

Flierl, G. R. (1981). Particle motions in large-amplitude wave fields. *Geophys. Astrophys. Fluid Dyn.* 18, 39–74. doi: 10.1080/03091928108208773

Garzoli, S. L., and Gordon, A. L. (1996). Origins and variability of the benguela current. *J. Geophys Res: Oceans* 101, 897–906. doi: 10.1029/95JC03221

Garzoli, S. L., Richardson, P. L., Duncombe Rae, C. M., Fratantoni, D. M., Goñi, G. J., and Roubicek, A. J. (1999). Three Agulhas rings observed during the Benguela Current Experiment. *J. Geophys Res: Oceans* 104, 20971–20985. doi: 10.1029/1999JC900060

Giulivi, C. F., and Gordon, A. L. (2006). Isopycnal displacements within the Cape Basin thermocline as revealed by the Hydrographic Data Archive. *Deep Sea Res. Part. I: Oceanograph Res. Papers* 53, 1285–1300. doi: 10.1016/j.dsr.2006.05.011

Goni, G. J., Garzoli, S. L., Roubicek, A. J., Olson, D. B., and Brown, O. B. (1997). Agulhas ring dynamics from TOPEX/POSEIDON satellite altimeter data. *J. Mar. Res.* 55, 861–883. doi: 10.1357/0022240973224175

Gordon, A. L., and Haxby, W. F. (1990). Agulhas eddies invade the south Atlantic: Evidence from Geosat altimeter and shipboard conductivity-temperature-depth survey. *J. Geophys Res: Oceans* 95, 3117–3125. doi: 10.1029/JC095iC03p03117

Gordon, A. L., Weiss, R. F., Smethie, W. M., and Warner, M. J. (1992). Thermocline and intermediate water communication between the south Atlantic and Indian oceans. *J. Geophys Res: Oceans* 97, 7223–7240. doi: 10.1029/92JC00485

Gründlingh, M. L. (1995). Tracking eddies in the southeast Atlantic and southwest Indian oceans with TOPEX/POSEIDON. *J. Geophys Res: Oceans* 100, 24977–24986. doi: 10.1029/95JC01985

Guerra, L. A. A., Paiva, A. M., and Chassignet, E. P. (2018). On the translation of Agulhas rings to the western South Atlantic Ocean. *Deep Sea Res. Part. I: Oceanograph Res. Papers* 139, 104–113. doi: 10.1016/j.dsr.2018.08.005

Hebert, D. (1988). The available potential energy of an isolated feature. *J. Geophys Res: Oceans* 93, 556–564. doi: 10.1029/JC093iC01p00556

Hernández-Guerra, A., Talley, L. D., Pelegrí, J. L., Vélez-Belchí, P., Baringer, M. O., Macdonald, A. M., et al. (2019). The upper, deep, abyssal and overturning circulation in the Atlantic Ocean at 30°S in 2003 and 2011. *Prog. Oceanogr.* 176, 102136. doi: 10.1016/j.pocean.2019.102136

Joyce, T. M., Patterson, S. L., and Millard, R. C. (1981). Anatomy of a cyclonic ring in the Drake Passage. *Deep Sea Res. Part. A. Oceanograph Res. Papers* 28, 1265–1287. doi: 10.1016/0198-0149(81)90034-0

Kamenkovich, V. M., Leonov, Y. P., Nechaev, D. A., Byrne, D. A., and Gordon, A. L. (1996). On the influence of bottom topography on the Agulhas eddy. *J. Phys. Oceanogr.* 26, 892–912. doi: 10.1175/1520-0485(1996)026<0892:OTIOBT>2.0.CO;2

Kang, D., and Curchitser, E. N. (2015). Energetics of eddy–mean flow interactions in the Gulf Stream region. *J. Phys. Oceanogr.* 45, 1103–1120. doi: 10.1175/JPO-D-14-0200.1

Laxenaire, R., Speich, S., Blanke, B., Chaigneau, A., Pegliasco, C., and Stegner, A. (2018). Anticyclonic eddies connecting the western boundaries of Indian and Atlantic Oceans. *J. Geophys Res: Oceans* 123, 7651–7677. doi: 10.1029/2018JC014270

Laxenaire, R., Speich, S., and Stegner, A. (2019). Evolution of the thermohaline structure of one Agulhas ring reconstructed from satellite altimetry and Argo floats. *J. Geophys Res: Oceans* 124, 8969–9003. doi: 10.1029/2018JC014426

Li, M., Pang, C., Yan, X., Zhang, L., and Liu, Z. (2023). Energetics of multiscale interactions in the Agulhas Retroflection Current system. *J. Phys. Oceanogr.* 53, 457–476. doi: 10.1175/JPO-D-21-0275.1

Liu, M., and Tanhua, T. (2021). Water masses in the Atlantic Ocean: Characteristics and distributions. *Ocean Sci.* 17, 463–486. doi: 10.5194/os-17-463-2021

Lutjeharms, J. R. (2006). *The Agulhas current retroflection* (Berlin, Heidelberg: Springer Berlin Heidelberg).

Lutjeharms, J. R. E. (2007). Three decades of research on the greater Agulhas Current. *Ocean Sci.* 3, 129–147. doi: 10.5194/os-3-129-2007

Lutjeharms, J. R. E., and Van Ballegooyen, R. C. (1988). The retroflection of the agulhas current. *J. Phys. Oceanogr.* 18, 1570–1583. doi: 10.1175/1520-0485(1988)018<1570:TROTAC>2.0.CO;2

Marshall, T. A., Sigman, D. M., Beal, L. M., Foreman, A., Martínez-García, A., Blain, S., et al. (2023). The Agulhas Current transports signals of local and remote Indian Ocean nitrogen cycling. *J. Geophys Res: Oceans* 128, e2022JC019413. doi: 10.1029/2022JC019413

Mason, E., Pascual, A., Gaube, P., Ruiz, S., Pelegrí, J. L., and Delepoulle, A. (2017). Subregional characterization of mesoscale eddies across the Brazil-Malvinas Confluence. *J. Geophys Res: Oceans* 122, 3329–3357. doi: 10.1002/2016JC012611

Matano, R. P., and Beier, E. J. (2003). A kinematic analysis of the Indian/Atlantic interocean exchange. *Deep Sea Res. Part. II: Topical Stud. Oceanograph* 50, 229–249. doi: 10.1016/S0967-0645(02)00395-8

McCartney, M. S., and Woodgate-Jones, M. E. (1991). A deep-reaching anticyclonic eddy in the subtropical gyre of the eastern South Atlantic. *Deep Sea Res. Part. A. Oceanograph Res. Papers* 38, S411–S443. doi: 10.1016/S0198-0149(12)80019-7

McDonagh, E. L., Heywood, K. J., and Meredith, M. P. (1999). On the structure, paths, and fluxes associated with Agulhas rings. *J. Geophys Res: Oceans* 104, 21007–21020. doi: 10.1029/1998JC900131

Mey, R. D., Walker, N. D., and Jury, M. R. (1990). Surface heat fluxes and marine boundary layer modification in the Agulhas Retroflection region. *J. Geophys Res: Oceans* 95, 15997–16015. doi: 10.1029/JC095iC09p15997

Nencioli, F., Dall'Olmo, G., and Quartly, G. D. (2018). Agulhas ring transport efficiency from combined satellite altimetry and Argo profiles. *J. Geophys Res: Oceans* 123, 5874–5888. doi: 10.1029/2018JC013909

Olson, D. B., and Evans, R. H. (1986). Rings of the agulhas current. *Deep Sea Res. Part. A. Oceanograph Res. Papers* 33, 27–42. doi: 10.1016/0198-0149(86)90106-8

Olson, D. B., Fine, R. A., and Gordon, A. L. (1992). Convective modifications of water masses in the Agulhas. *Deep Sea Res. Part. A. Oceanograph Res. Papers* 39, S163–S181. doi: 10.1016/S0198-0149(11)80010-5

Penven, P., Halo, I., Pous, S., and Marié, L. (2014). Cyclogeostrophic balance in the Mozambique channel. *J. Geophys Res: Oceans* 119, 1054–1067. doi: 10.1002/2013JC009528

Pichevin, T., Nof, D., and Lutjeharms, J. (1999). Why are there Agulhas rings? *J. Phys. Oceanogr.* 29, 693–707. doi: 10.1175/1520-0485(1999)029<0693:WATAR>2.0.CO;2

Poole, R., and Tomczak, M. (1999). Optimum multiparameter analysis of the water mass structure in the Atlantic Ocean thermocline. *Deep Sea Res. Part. I: Oceanograph Res. Papers* 46, 1895–1921. doi: 10.1016/S0967-0637(99)00025-4

Rae, C. M. D., Garzoli, S. L., and Gordon, A. L. (1996). The eddy field of the southeast Atlantic Ocean: A statistical census from the Benguela Sources and Transports Project. *J. Geophys Res: Oceans* 101, 11949–11964. doi: 10.1029/95JC03360

Richardson, P. L. (2007). Agulhas leakage into the Atlantic estimated with subsurface floats and surface drifters. *Deep Sea Res. Part. I: Oceanograph Res. Papers* 54, 1361–1389. doi: 10.1016/j.dsr.2007.04.010

Russell, J., Sarmiento, J., Cullen, H., Hotinski, R., Johnson, K., Riser, S., et al. (2014). The southern ocean carbon and climate observations and modeling program (SOCCOM). *Ocean Carbon Biogeochem Newsl.* 7, 1–5. doi: 10.1016/j.pocean.2023.103130

Sangrà, P., Auladell, M., Marrero-Díaz, A., Pelegrí, J. L., Fraile-Nuez, E., Rodríguez-Santana, A., et al. (2007). On the nature of oceanic eddies shed by the Island of Gran Canaria. *Deep Sea Res. Part. I: Oceanograph Res. Papers* 54, 687–709. doi: 10.1016/j.dsr.2007.02.004

Sangrà, P., Pelegrí, J. L., Hernández-Guerra, A., Arregui, I., Martín, J. M., Marrero-Díaz, A., et al. (2005). Life history of an anticyclonic eddy. *J. Geophys Res: Oceans* 110, 1–19. doi: 10.1029/2004JC002526

Sarmiento, J. L., Johnson, K. S., Arteaga, L. A., Bushinsky, S. M., Cullen, H. M., Gray, A. R., et al. (2023). The Southern Ocean carbon and climate observations and modeling (SOCCOM) project: A review. *Prog. Oceanogr.* 219, 103130. doi: 10.1016/j.pocean.2023.103130

Schmid, C., Boebel, O., Zenk, W., Lutjeharms, J. R. E., Garzoli, S. L., Richardson, P. L., et al. (2003). Early evolution of an agulhas ring. *Deep Sea Res. Part. II: Topical Stud. Oceanograph* 50, 141–166. doi: 10.1016/S0967-0645(02)00382-X

Schott, F. A., and McCreary, J. P. (2001). The monsoon circulation of the Indian Ocean. *Prog. Oceanogr.* 51, 1–123. doi: 10.1016/S0079-6611(01)00083-0

Schouten, M. W., de Ruijter, W. P. M., van Leeuwen, P. J., and Lutjeharms, J. R. E. (2000). Translation, decay and splitting of Agulhas rings in the southeastern Atlantic Ocean. *J. Geophys Res: Oceans* 105, 21913–21925. doi: 10.1029/1999JC000046

Simpson, J. J., Dickey, T. D., and Koblinsky, C. J. (1984). An offshore eddy in the California current system Part I: Interior dynamics. *Prog. Oceanogr.* 13, 5–49. doi: 10.1016/0079-6611(84)90004-1

Souza, J. M. A. C., de Boyer Montégut, C., Cabanes, C., and Klein, P. (2011). Estimation of the Agulhas ring impacts on meridional heat fluxes and transport using ARGO floats and satellite data. *Geophys. Res. Lett.* 38, n/a–n/a. doi: 10.1029/2011GL049359

Stramma, L., and England, M. (1999). On the water masses and mean circulation of the South Atlantic Ocean. *J. Geophys Res: Oceans* 104, 20863–20883. doi: 10.1029/1999JC900139

Tokos, K. S., and Rossby, T. (1991). Kinematics and dynamics of a mediterranean salt lens. *J. Phys. Oceanogr.* 21, 879–892. doi: 10.1175/1520-0485(1991)021<0879:KADOAM>2.0.CO;2

Valencia, L. P., Rodríguez-Santana, Á., Aguiar-González, B., Arístegui, J., Álvarez-Salgado, X. A., Coca, J., et al. (2025). Mesoscale dynamics of an intrathermocline eddy in the Canary Eddy Corridor. *Ocean Sci.* 21, 2305–2344. doi: 10.5194/os-21-2305-2025

Van Aken, H. M., Van Veldhoven, A. K., Veth, C., De Ruijter, W. P. M., Van Leeuwen, P. J., Drijfhout, S. S., et al. (2003). Observations of a young Agulhas ring, Astrid, during MARE in March 2000. *Deep Sea Res. Part. II: Topical Stud. Oceanograph* 50, 167–195. doi: 10.1016/S0967-0645(02)00383-1

Van Ballegooyen, R. C., Gründlingh, M. L., and Lutjeharms, J. R. E. (1994). Eddy fluxes of heat and salt from the southwest Indian Ocean into the southeast Atlantic Ocean: A case study. *J. Geophys Res: Oceans* 99, 14053–14070. doi: 10.1029/94JC00383

Voss, M., Bange, H. W., Dippner, J. W., Middelburg, J. J., Montoya, J. P., and Ward, B. (2013). The marine nitrogen cycle: recent discoveries, uncertainties and the potential relevance of climate change. *Philos. Trans. R. Soc. B. Biol. Sci.* 368, 20130121. doi: 10.1098/rstb.2013.0121

Weijer, W., De Ruijter, W. P. M., Dijkstra, H. A., and van Leeuwen, P. J. (1999). Impact of interbasin exchange on the atlantic overturning circulation. *J. Phys. Oceanogr.* 29, 2266–2284. doi: 10.1175/1520-0485(1999)029<2266:IOIEOT>2.0.CO;2